hydrogen

MDPI

Article

Nanoscale Nickel–Chromium Powder as a Catalyst in Reducing the Temperature of Hydrogen Desorption from Magnesium Hydride

Alan Kenzhiyev *, Viktor N. Kudiiarov, Alena A. Spiridonova, Daria V. Terenteva, Dmitrii B. Vrublevskii, Leonid A. Svyatkin, Dmitriy S. Nikitin and Egor B. Kashkarov

Division for Experimental Physics, School of Nuclear Science & Engineering, National Research Tomsk Polytechnic University, 634050 Tomsk, Russia; kudiyarov@tpu.ru (V.N.K.); aas374@tpu.ru (A.A.S.); dvt17@tpu.ru (D.V.T.); dbv2@tpu.ru (D.B.V.); svyatkin@tpu.ru (L.A.S.); nikitindmsr@yandex.ru (D.S.N.); ebk@tpu.ru (E.B.K.)

* Correspondence: kenzhiyev@tpu.ru; Tel.: +7-999-178-2720

Abstract

The composite material MgH_2-EEWNi-Cr (20 wt. %) with a hydrogen content of 5.2 ± 0.1 wt.% is characterized by improved hydrogen interaction properties compared to the original MgH_2. The dissociation of the material occurs in three temperature ranges (86–117, 152–162, and 281–351 °C), associated with a complex of effects consisting of changes in the specific surface area of the material, alterations in the crystal lattice during ball milling, and changes in the electronic structure in the presence of a Ni–Cr catalyst, based on first-principles calculations. The decrease in desorption activation energy (E_d = 65–96 ± 1 kJ/mol, ΔE_d = 59–90 kJ/mol) is due to the catalytic effect of N–Cr, leading to a faster decomposition of the hydride phase. Based on the results of ab initio calculations, Ni–Cr on the MgH_2 surface leads to a significant decrease in hydrogen binding energy (ΔE_b = 60%) compared to pure magnesium hydride due to the formation of Ni–H and Cr–H covalent bonds, which reduces the degree of H–Mg ionic bonding. The results obtained allow us to expand our understanding of the mechanisms of hydrogen interaction with storage materials and the possibility of using these as mobile hydrogen storage and transportation materials.

Keywords: hydrogen storage material; magnesium; nickel; chromium; electrical explosion of wires; ab initio; DFT

check for updates

Academic Editor: Kaveh Edalati

Received: 20 November 2025
Revised: 13 December 2025
Accepted: 15 December 2025
Published: 17 December 2025

Citation: Kenzhiyev, A.; Kudiiarov, V.N.; Spiridonova, A.A.; Terenteva, D.V.; Vrublevskii, D.B.; Svyatkin, L.A.; Nikitin, D.S.; Kashkarov, E.B. Nanoscale Nickel–Chromium Powder as a Catalyst in Reducing the Temperature of Hydrogen Desorption from Magnesium Hydride. *Hydrogen* **2025**, *6*, 123. https://doi.org/10.3390/hydrogen6040123

Copyright: © 2025 by the authors. Licensee MDPI, Basel, Switzerland. This article is an open access article distributed under the terms and conditions of the Creative Commons Attribution (CC BY) license (https://creativecommons.org/licenses/by/4.0/).

1. Introduction

Research into storage materials, particularly metal hydrides, has attracted the attention of scientists around the world in recent years. The search for alternative energy sources has been prompted by scientific groups' predictions about the limited availability of traditional energy sources. The use of hydrogen as an energy source is the most promising due to its high energy density, its widespread availability, and the absence of harmful emissions during its use, extraction, and production [1–4].

Hydrogen can be used in the form of gas (low gravimetric density and high pressure), in the form of liquid (strict adherence to temperature conditions), and in a chemically bound state. The latter storage method meets most of the properties of the most effective hydrogen storage material, as defined by the Ministry of Hydrogen Energy.

High gravimetric density, acceptable operating temperatures, and fast sorption and desorption kinetics are characteristics inherent to solid storage materials. Studying the mechanisms, establishing patterns, and improving the characteristics of hydrogen interaction with these materials are among the main challenges in this field. Various research groups around the world [5–11] have studied metal hydrides, carbon nanotubes, zeolites, intermetallics, and other types of metals. However, the diversity of the materials studied and the different approaches used do not allow for a complete explanation of the patterns of behavior of these materials. This was the basis for this study—comparing experimental data with theoretical material for a more complete understanding of the processes involved. Research on carbon nanomaterials [12–15] has established their particular effectiveness on par with MOFs (metal–organic framework structures) [16–28], nanorods, and zeolites [29–31]. Such materials allow certain characteristics of effective storage devices to be achieved at an acceptable level. They have low density, high specific surface area, and high reproducibility. However, their synthesis is expensive and labor-intensive [32].

Further, scientists' attention was drawn to the study of metal hydrides, one of the most prominent examples of which is $LaNi_5$ [33–38]. Despite its low hydrogen content by mass (about 1.2–1.4 wt.%), it has excellent cyclic stability at room temperature. Since it is a rare-earth compound with high density, its use is limited by its high cost. For this reason, one of the most studied metal hydrides in recent decades is magnesium hydride. Its main advantages are high gravimetric density in terms of hydrogen (7.66 wt.%), low density (1.738 g/cm^3), abundance in the Earth's crust, and low cost [39,40]. At the same time, it has a sufficiently high stability of hydrogen–metal bonds, as a result of which it has a high hydrogen release temperature of 400 °C. Improving this characteristic can be achieved by various methods, such as the use of transition metals and their oxides, varying the synthesis parameters, reducing the dispersion of materials, adding catalysts, and so on [41–43]. In our previous studies, using a Ni catalyst, we observed that the formation of the Mg_2Ni phase, which has a high affinity for hydrogen, allows the formation of the hydride phase at lower energies. This is described by the fact that this phase is acts like a "hydrogen pump" that creates local diffusing pathways in the crystal lattice of the material. The resulting Mg_2NiH_4 phase is in addition easily dissociated due to the same effects observed in our previous studies [2,4].

The work of authors M. Polanski et al. [44] demonstrates rather good cyclic stability of a composite based on magnesium hydride and chromium oxide (Cr_2O_3) at 325 °C. The authors present the results of 150 hydrogenation cycles during which the capacity of the material decreases from 5.2 to 4.6 wt.%. In a similar study M. Polanski and J. Bystrzycki [45] studied the effects of adding different metal oxides on the hydrogen absorption properties of materials. One of the main results was that the addition of chromium oxide powder significantly accelerates the reaction rate of material interaction with hydrogen. This applies to both the sorption and desorption processes. About 6 wt.% of hydrogen was desorbed in 5 min at a temperature of 325 °C and a pressure of 1 atm. The study of the same chromium oxide powder by the authors Pukazhselvan et al. [46] demonstrates a positive effect both in decreasing the desorption temperature and in accelerating the reaction kinetics. Several studies on nickel [47–49] demonstrate a positive effect in reducing the temperature of hydrogen desorption from the material. As mentioned above, this is due to the formation of a special phase, which acts like a "hydrogen pump" and allows the formation of hydride phases at much lower energies.

To summarize the above, there is a particular need at present to find and develop effective materials for storing and transporting hydrogen by evaluating characteristics such as their performance, cost, and practicality of use. This is a priority area of research in this field. Despite the advantages of carbon materials and MOFs in terms of high specific surface

area, their use is limited by the complexity of synthesis and the scalability of production technology. In contrast, intermetallic compounds such as $LaNi_5$ demonstrate excellent cyclic stability but do not have a high gravimetric density (1.5 wt.% of hydrogen) and are not economically viable. Magnesium hydride, which has been studied in recent decades, including in this work, has a number of advantages listed above in the text. Based on the experience of previous studies, special attention was paid in this work to catalytic additives, in particular nanoscale nickel–chromium powder produced by the method of electrical explosion of wires. Our research group decided to establish patterns and explain the mechanisms of such behavior in correlation between experimental and theoretical data. The fundamental novelty of this scientific work is the study of the influence of nanoscale additives produced by the method of electrical explosion of wires as catalysts for reducing the operating temperatures of magnesium hydride. A deeper understanding of these processes and a comprehensive approach to solving current issues will bring us closer to the development of the most effective storage materials for use as mobile supplies for hydrogen storage and transport.

2. Materials and Methods

2.1. Material Preparation

The powder used, MPF-4 (Russia, Tomsk, "Velund steel"), has a purity of 99.2% and a particle size from 50 to 300 microns. The nickel–chromium powder has nanoscale particles up to 100 nm. The initial magnesium hydride and composites were prepared and studied using the automated Gas Reaction Automated Machine (GRAM50) complex developed at the Department of Experimental Physics of Tomsk Polytechnic University. Before the hydrogenation process, magnesium powder was pre-activated in the planetary ball mill AGO-2 (Novosibirsk, Russia) at a rotation speed of 900 rpm and a total operating time of 120 min. Next, the activated powder was subjected to a hydrogenation process at a temperature of 663 K and a pressure of 30 atmospheres for 300 min. Mechanical synthesis was carried out using a planetary ball mill, AGO-2. Such experimental parameters are based on previous studies by our and similar scientific groups and are optimal for this process. The amount of nanoscale nickel–chromium powder added was 20 wt.%. The parameters of mechanical synthesis were chosen to be the same as during the activation of the initial magnesium metal powder. However, the ratio of the mass of the balls to the powder was not 10:1, but 20:1. All procedures for loading and unloading samples were carried out using a SPEKS GB02M glove box in an inert argon atmosphere. Activation and synthesis were carried out in an inert atmosphere.

2.2. Analysis and Characterization

The hydrogen concentration was measured by melting samples in an inert gas atmosphere using a RHEN602 hydrogen analyzer (LECO Corporation, St. Joseph, MI, USA).

The microstructure of the composite was studied using a TESCAN VEGA 3 SBU scanning electron microscope (Tescan Orsay Holding a.s., Brno, Czech Republic). The elemental composition of the composite was analyzed by energy-dispersive X-ray spectroscopy on an X-Max 50 X-ray spectrometer (Oxford Instruments plc, Abingdon, UK).

The crystal structure of the samples was analyzed by X-ray diffraction (XRD) in the scanning range (5–80)° using XRD-7000S (Shimadzu, Kyoto, Japan). The diffractometer was operated in the Bragg–Brentano configuration with a Cu Kα anode (λ = 0.154 nm) operating at 40 kV and 30 mA.

Low-temperature sorption of N_2 was used to characterize the textural properties of samples at cryogenic temperature using a 3Flex automated gas adsorption analyzer (Micromeritics Instruments Corporation, Norcross, GA, USA). The values of the surface

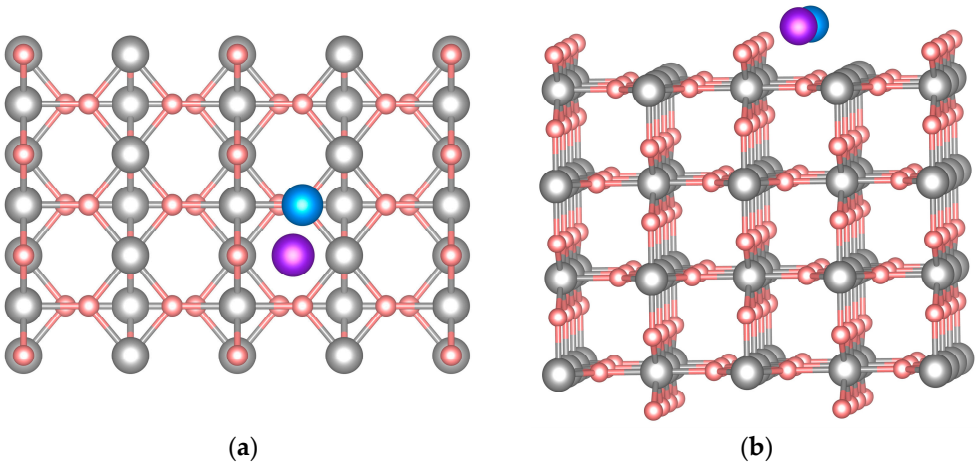
area were calculated by linearization using the coordinates of the Brunauer–Emmett–Teller (BET) equation in the range of relative pressure from 0.05 to 0.3. To plot the mesopore size distribution, the Barrett–Joyner–Halenda (BJH) method was used with the analysis of the isotherm desorption branch. The micropore distribution was calculated using the Horvath–Kavazoe method. The samples were degassed in vacuum at a temperature of 573 K for 10 h before the measurements.

The method of temperature-programmed desorption (TPD) of hydrogen at heating rates of 2, 4, 6, and 8 °C/min to a temperature of 723 K in the experimental chamber with simultaneous data collection of desorption spectra using a quadrupole mass spectrometer RGA100 (Stanford Research Systems, Sunnyvale, CA, USA) was used to estimate the state of hydrogen in the material. Each of the analyses performed was carried out more than five times. The experimental data described in the article are average values for the materials studied. The data presented in this paper are the average results from the data set obtained. Each measurement was taken at least five times to ensure the most accurate result.

2.3. Methods and Calculation Details

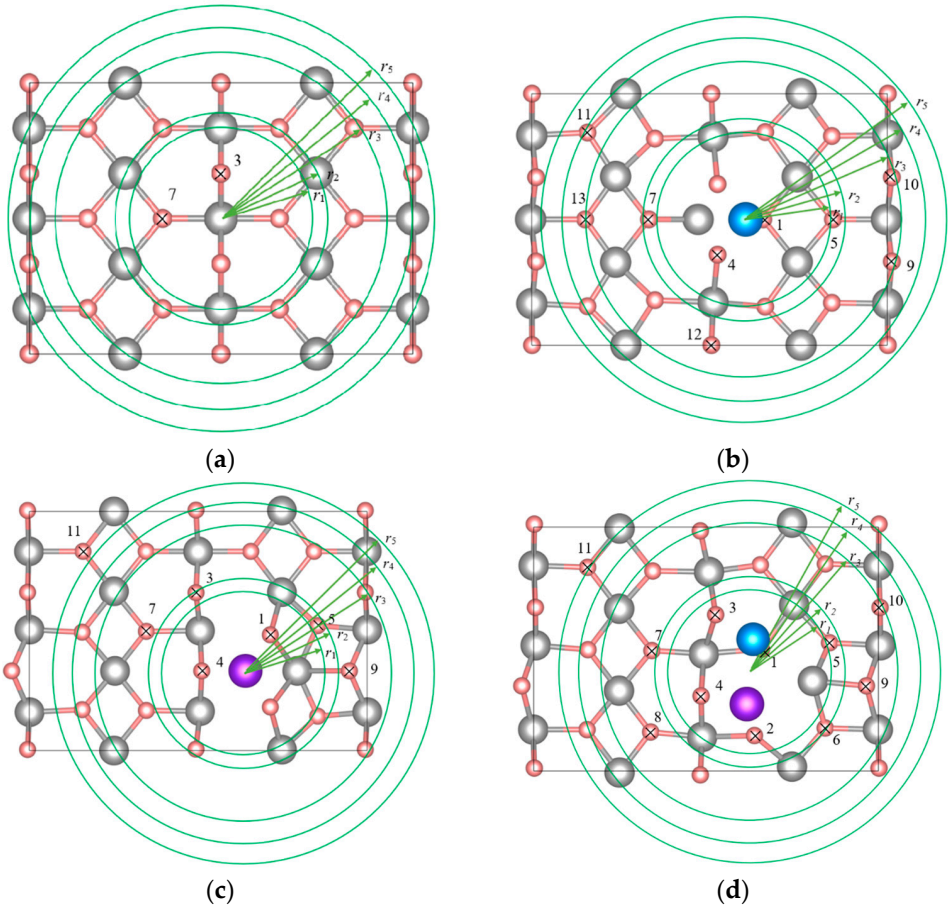
Within the framework of the electron density functional theory (DFT) using the method of projected augmented plane waves implemented in the ABINIT program package [50,51], calculations of hydrogen binding energies on the pristine β-MgH_2 (110) surface as well as in the presence of adsorbed Cr and Ni atoms were performed. The generalized gradient approximation in the form of Perdue, Burke, and Ernzerhof [52] was employed to describe exchange and correlation effects. A four-layer $Mg_{48}H_{96}$ film in the 2 × 3 structure (supercell dimensions are 12.72 × 9.01 Å) was used to study the interaction of Cr and Ni atoms with the (110) surface of β-MgH_2 with a TiO_2-like structure (Figure 1). As shown in Figure 1b, each atomic layer of the computational supercell contains 12 magnesium and 24 hydrogen atoms, which ensures a stoichiometric system. The vacuum layer separating the $Mg_{48}H_{96}$ film systems in adjacent computational cells was set to approximately 15 Å. This vacuum layer allows us to prevent interactions between the adsorbed Cr and Ni atoms and the surface Mg and H atoms in neighboring supercells. In this work, 6 nonequivalent adsorption positions of Ni and Cr atoms on the (110) MgH_2 surface were considered. The adsorption energies for the nickel and chromium vary in the ranges from 1.0 eV to 4.4 eV and from 4.5 eV to 7.3 eV, respectively. In this work, we consider the energetically most favorable positions for a single nickel or chromium atom, which are presented in Figure 2. These same positions were used for co-adsorption of both Ni and Cr as well. Figure 2 shows the top view of the (110) surface, illustrating the nonequivalent positions of H atoms and the adsorption sites of Cr and Ni atoms with the highest adsorption energies. Relaxation was considered complete when the force acting on each atom was less than 10 meV/Å. At each iteration of self-consistency, the eigenvalues of the Hamiltonian were calculated on a 6 × 8 × 1 grid of k-points generated by the Monkhorst–Pack scheme in the entire Brillouin zone of the described supercells. The cutoff energy at the wave function decomposition by the plane wave basis was 700 eV. To analyze the nature of the interaction of nickel and chromium with hydrogen on the β-MgH_2 (110) surface, the valence electron distribution was studied and Bader charge calculations [53] were performed.

The choice of the 2 × 3 supercell size and slab thickness was validated through a series of convergence tests. Increasing the slab thickness from 4 to 6 atomic layers and the 2D dimensions from 12.72 × 9.01 Å to 15.90 × 12.01 Å resulted in a change in hydrogen binding energies of less than 5 meV. Such negligible changes in hydrogen binding energies verify that the selected cell parameters are appropriate.



(**a**) (**b**)

Figure 1. Top view (**a**) and side view (**b**) of the supercell modeling the (110) surface of β-MgH_2. The atoms of Mg, H, Ni, and Cr are colored as gray, pink, blue, and purple, respectively.



(**a**) (**b**) (**c**) (**d**)

Figure 2. Top view of the (110) β-MgH_2 film: pristine surface (**a**); surface with an adsorbed Ni atom (**b**); surface with an adsorbed Cr atom (**c**); surface with co-adsorbed Cr and Ni atoms (**d**). The atoms of Mg, H, Ni, and Cr are colored as gray, pink, blue, and purple, respectively. Concentric regions with radii r_1, r_2, … r_5 are drawn on the MgH_2 surface relative to the mass center of the surface impurities. Nonequivalent surface H atoms are marked by crosshairs and numbered for ease of discussion.

The hydrogen binding energy E_b on the (110) surface of β-MgH_2 was calculated using the following expression:

$$E_{\mathrm{b}} = E_{\mathrm{tot}}\left(\mathrm{Mg_nH_{2n-1}Ni_xCr_y}\right) + \frac{1}{2}E_{\mathrm{tot}}\left(\mathrm{H_2}\right) - E_{\mathrm{tot}}\left(\mathrm{Mg_nH_{2n}Ni_xCr_y}\right) \quad (1)$$

where $E_{tot}(Mg_nH_{2n}Ni_xCr_y)$ is the total energy of the magnesium hydride supercell containing n Mg atoms and adsorbed x Ni atoms and y Cr atoms (in the computational cell, x and y take values of 0 or 1). $E_{tot}(Mg_nH_{2n-1}Ni_xCr_y)$ is the total energy of the magnesium hydride supercell from which one of the surface H atoms has been removed, and $E_{tot}(H_2)$ is the total energy of the hydrogen molecule.

The value of E_b should be interpreted as an indication of how hydrogen atoms promote hydrogen release. Positive values of E_b indicate that the removal of the hydrogen atom from the system requires energy consumption; i.e., such atoms are strongly bound within the surface. Negative values, in contrast, imply that the removal of the hydrogen atom is thermodynamically favorable. Nevertheless, even in the case of negative E_b, hydrogen release does not necessarily proceed spontaneously, as it requires overcoming significant activation energy. Thus, the value of E_b reflects the strength of hydrogen retention on the surface: the smaller its value, the weaker the interaction. In particular, hydrogen atoms with negative E_b are the most prone to desorption and are likely to be released first under external perturbations.

In order to verify the computational parameters, the influence of k-points and cutoff energy on the computational accuracy was investigated. Thus, the change in the hydrogen binding energy for the system studied did not exceed the value of 1 meV with the increasing of the *k*-point mesh grid from 6 × 8 × 1 to 8 × 10 × 1 and cutoff energy from 700 eV to 900 eV. This change is insignificant and allows us to claim this as an accurate description of interaction between additives and hydrogen atoms on the MgH_2 (110) surface.

3. Results

3.1. Composite Characterization

Figure 3 shows the XRD results of ball-milled MgH_2-EEWNi-Cr. The main components of the ball-milled MgH_2-EEWNi-Cr sample were Mg, MgH_2, and Ni–Cr.

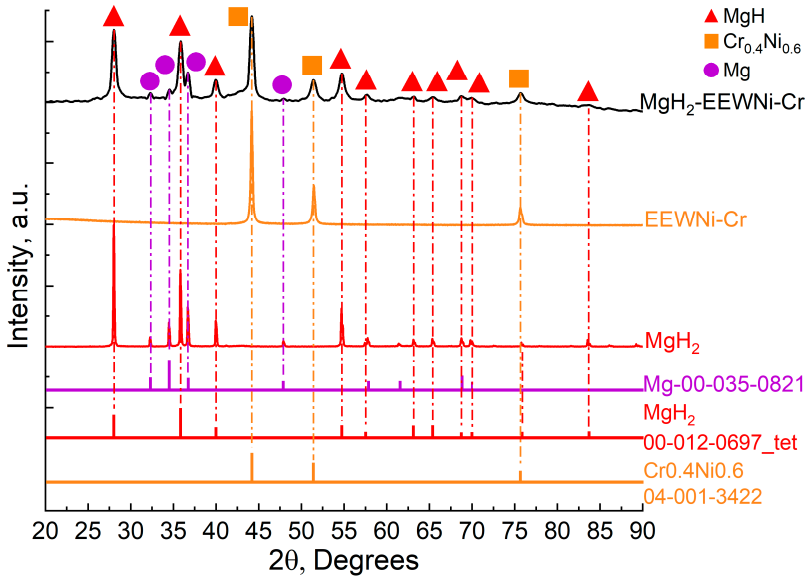


Figure 3. XRD patterns of magnesium hydride and MgH_2-EEWNi-Cr composite with corresponding JCPDS cards.

Diffraction analysis of the materials made it possible to determine the composition and did not reveal the presence of extraneous phases. The magnesium hydride lattice has a tetragonal rutile-type structure; the main phase in the prepared magnesium hydride was the β-MgH_2 phase. The phases found in the composite material are HCP Mg, β-MgH_2, and CrNi with a BCC lattice for chromium and FCC lattice for nickel. Characteristic

peaks for CrNi are observed at diffraction angles 44.5°, 51.8°, and 75.4°. In addition, peak broadening is observed in the composite, which is due to the accumulation of defects during the milling process. To clarify the structural characteristics of the crystal lattice of the materials under study, Table 1 below presents the calculated microstrain values using PowderCell24 (2.4) software.

Table 1. Values of microstrains in materials.

Sample	Phases (PowderCell24 cards)	Phase Content, ±0.2 vol.%	Lattice Parameters, ±0.0005 Å	Crystalline Size, ±0.05 nm	Microstrains, ±0.0003 Δd/d
MgH_2	Mg-00-035-0821	16.6	a = 3.1998 c = 5.1978	36.84	0.0011
	MgH_2-00-012-0697_tet	83.4	a = 4.5003 c = 3.0142	64.98	0.0016
EEWNi-Cr	Cr0.4Ni0.6-04-001-3422	100	a = 3.5540	40.49	0.0004
MgH_2–20 wt.% EEWNi-Cr	Mg-00-035-0821	9.7	a = 3.1950 c = 5.2020	7.37	0.0054
	MgH_2-00-012-0697_tet	85.8	a = 4.5070 c = 3.0110	40.95	0.0062
	Cr0.4Ni0.6-04-001-3422	4.5	a = 3.5490	23.3	0.0011

Based on the results of microstrain analysis in the material from Table 1, it can be established that the number of internal strains in the crystal lattice increases almost by a factor of four. The data obtained on changes in the crystalline structure of the material indicate a more developed defect structure and a decrease in the dispersibility of the ground materials. All this contributes to easier bonding of hydrogen with magnesium atoms, as well as their permeation/release into/from the bulk. During the analysis of diffraction curves, no alloy compounds between magnesium and Ni–Cr were detected. The $Cr_{0.4}Ni_{0.6}$ phase is clearly visible in the composite material. It is a direct factor influencing the change in the discussed properties of magnesium. A comprehensive approach combining experimental and theoretical data allows us to establish the nature of the mechanism of this effect. In our previous studies [2,4], we found a significant influence on the change in hydrogen desorption kinetics, which was partly related to the formation of the Mg_2NiH_4 phase. The phase acted as a "hydrogen pump" [2,4]—nickel catalyzed the hydrogen sorption properties of Mg/MgH_2. The principle of this mechanism is described in more detail in another study and is also presumably one of the fundamental principles for the MgH_2-EEWNi-Cr composite discussed in this study.

Figure 4 shows microphotographs of EEWNi-Cr, MgH_2, and the MgH_2-EEWNi-Cr composite obtained using a tunneling electron microscope (TEM) and scanning electron microscope (SEM), as well as histograms of particle size distribution and element distribution maps.

From the images presented above, most of the magnesium hydride particles are agglomerates with an average size of about (50 ± 12.5) μm, with the largest particles reaching about 200 μm in size. In Figure 4f, the particle size is reduced significantly to (0.1 ± 0.0125) μm, which is due to milling in a planetary mill and the co-milling of magnesium powder with balls and nanoscale nickel–chromium powder. This reduction in size improves the hydrogen interaction characteristics of the material.

Figure 5 and Table 2 show the energy-dispersive analysis data for the initial EEWNi-Cr powder.

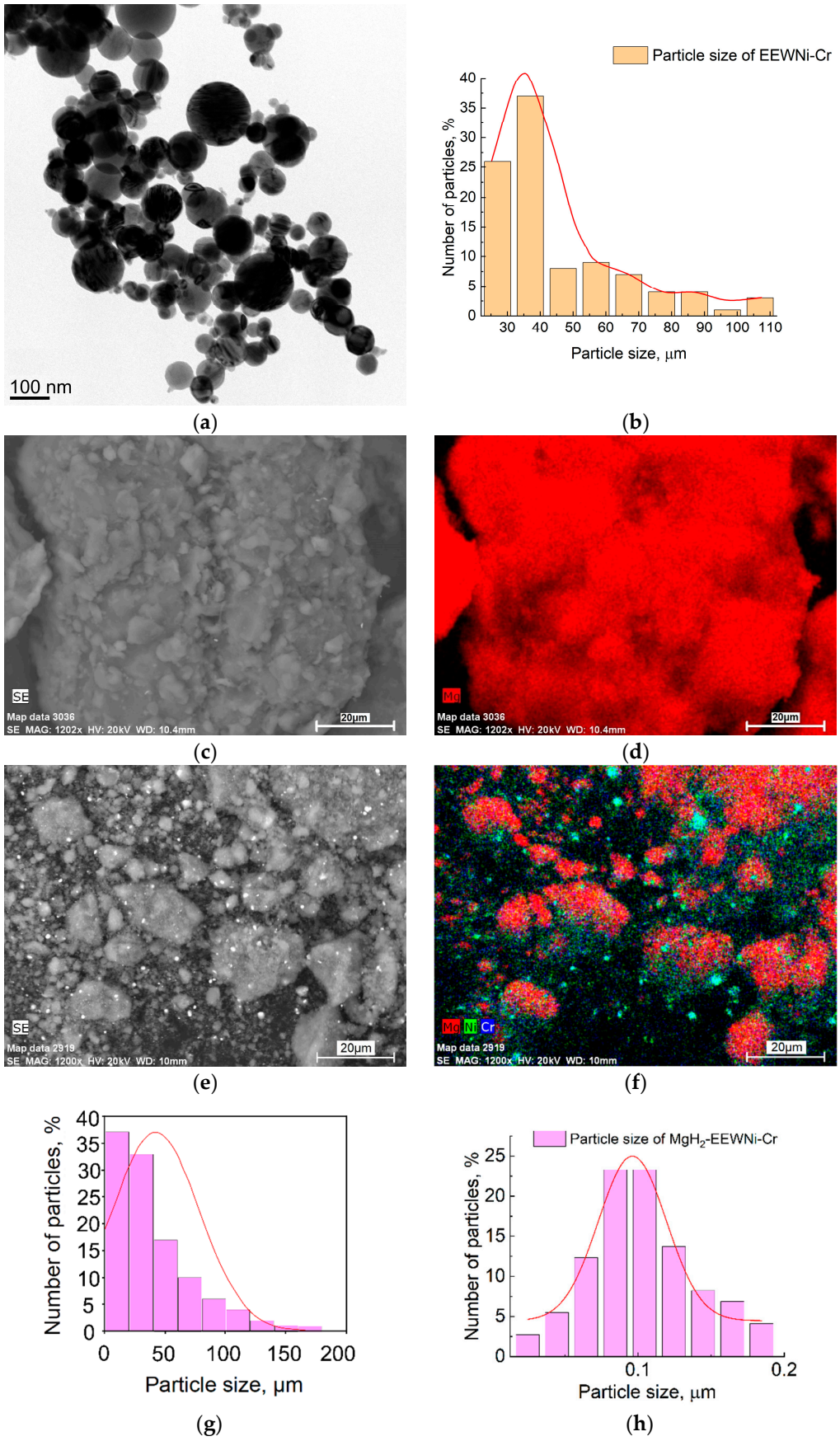


Figure 4. TEM micrographs of EEWNi-Cr (**a**), and SEM micrographs of MgH_2 (**c**) and the MgH_2-EEWNi-Cr (**e**) composite with the corresponding elemental mapping analysis (EDX) (**d**,**f**) and particle size distribution for EEWNi-Cr (**b**), MgH_2 (**g**), and the composite (**h**).

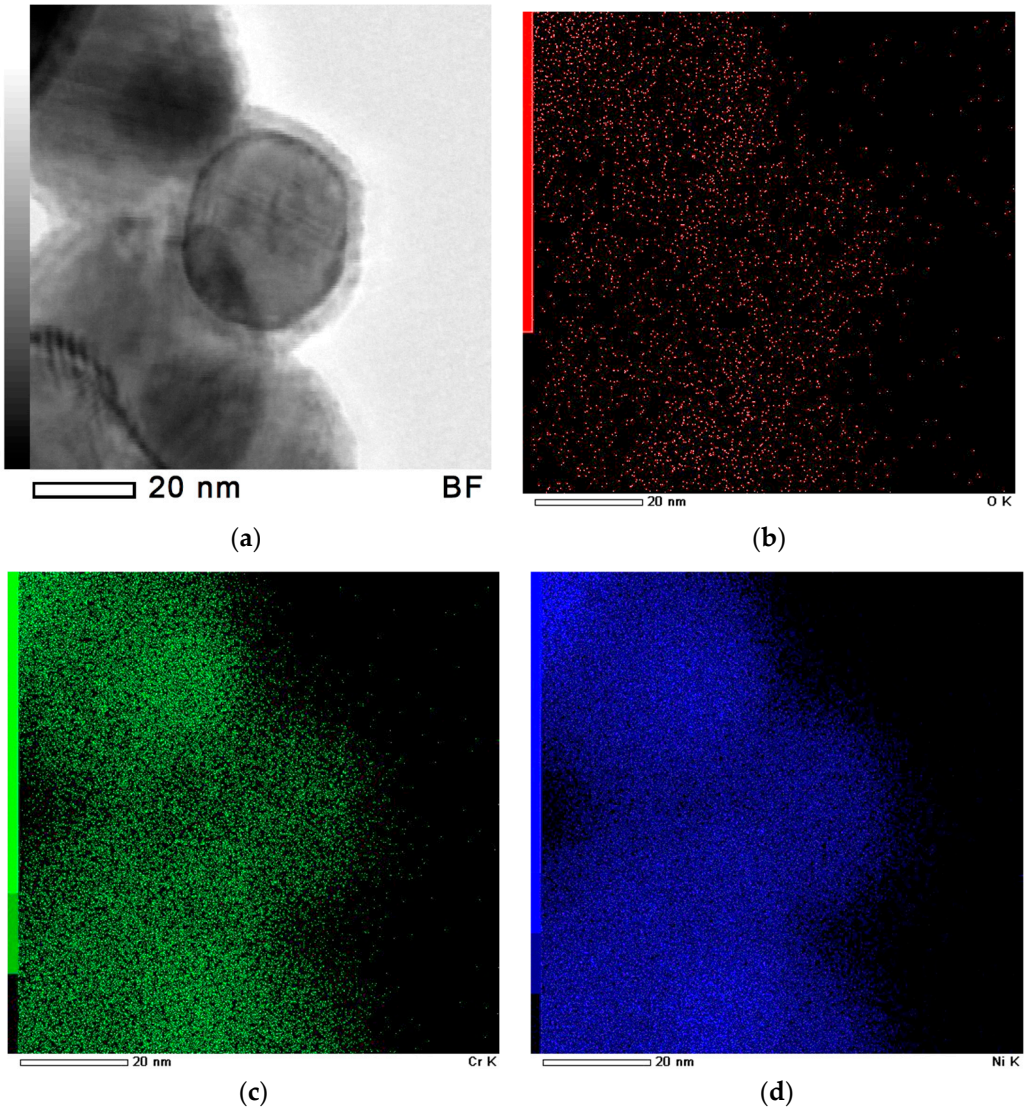


Figure 5. Energy-dispersive spectroscopy for EEWNi-Cr powder: (**a**) image of the EEWNi-Cr particles; distribution maps of (**b**) oxygen, (**c**) chromium, and (**d**) nickel.

Table 2. Results of energy-dispersive analysis for EEWNi-Cr.

Element	Mass%	Atom%
O	1.41	4.86
Cr	23.39	24.68
Ni	75.20	70.46
Total	100.00	100.00

A particle of the original nickel–chromium powder is a sphere with an oxide passivation film around it. From the element distribution maps for the material, nickel, chromium, and oxygen can be clearly seen, and are evenly distributed.

The nitrogen absorption method (BET method) allowed us to study the textural properties of the materials of this work. Adsorption–desorption isotherms at 573 K for magnesium hydride and the composite were determined. Figure 6 shows the isotherms, in which larger hysteresis is well observed for the composite than for the original magnesium hydride. This behavior of the material is due to the increase in the interface area, thereby increasing the number of diffusing pathways in the crystalline lattice of the material. On the other hand, the main adsorption of N_2 on the adsorption isotherms for the MgH_2-

EEWNi-Cr composite starts at a slightly lower relative pressure ($P/P_0 \approx 0.6$). The amount of adsorbed nitrogen in the composite material is greater by tens of times. The surface area (Table 3) for MgH_2-EEWNi-Cr is 3–5 times larger. Larger average pore diameter and pore volume additionally characterize the material.

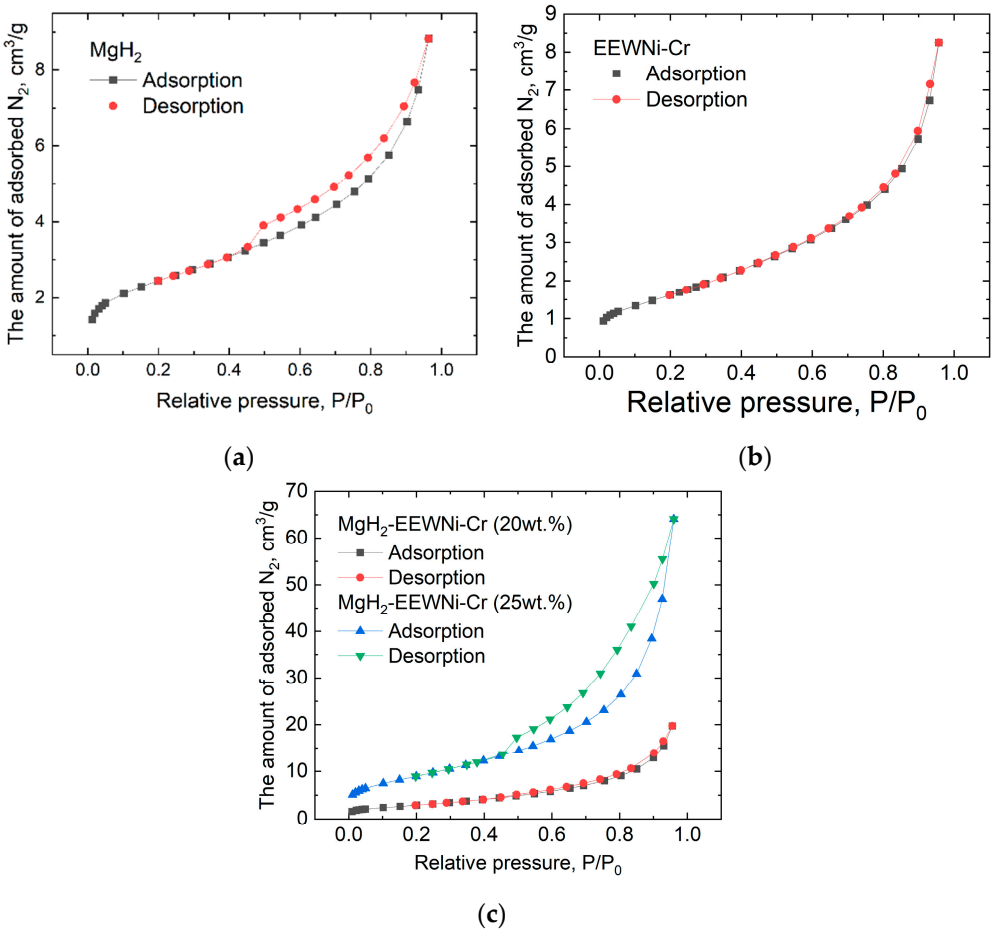


Figure 6. N_2 adsorption–desorption isotherms for MgH_2 (**a**), EEWNi-Cr (**b**), and MgH_2-EEWNi-Cr (**c**).

Table 3. BET analysis parameters.

Sample	Degassing Vacuum	BET Surface Area, m^2/g	Total Pore Volume, cm^3/g	Average Pore Diameter, nm
MgH_2 (0.4347 g)	10 h 573 K	8.5	0.014	6.4
EEWNi-Cr (0.8781 g)		6.2	0.013	8.1
MgH_2-EEWNi-Cr (20 wt.%) (0.3409 g)		10.6	0.031	11.5
MgH_2-EEWNi-Cr (25 wt.%) (0.2321 g)		28.5	0.099	13.9

Thus, the co-milling of MgH_2 and EEWNi-Cr powders allows us to significantly increase the BET surface area and N_2 absorption, which may be a consequence of the milling process effect, as well as the specific features of the "core-shell" structure appearance. The amount of powder used for BET analysis is usually between 0.2 and 1 g. The porosity of the materials studied is represented by the total pore volume and average pore diameter values. For composites, a significant change in material porosity can be observed, as well as in specific surface area (Table 3).

3.2. Hydrogen Storage Properties of Composite

The study of temperature-programmable desorption (Figure 7) demonstrated the positive effect of adding nickel–chromium powder. In this case, the desorption process was divided into three stages in different temperature regions, which are further designated as low-, medium-, and high-temperature regions. The dissociation of the hydride occurs in the high-temperature region, which is due to the high stability of the hydrogen bonds in magnesium. The temperature can be reduced by ball milling in a planetary ball mill. This is demonstrated by the high-temperature decomposition region of the composite (281–351 °C). This area is directly related to the decomposition of the magnesium hydride phase; the other two areas (low and medium) are related to the catalytic effect of nickel–chromium powder and the decomposition of the hydride phase of the composite material.

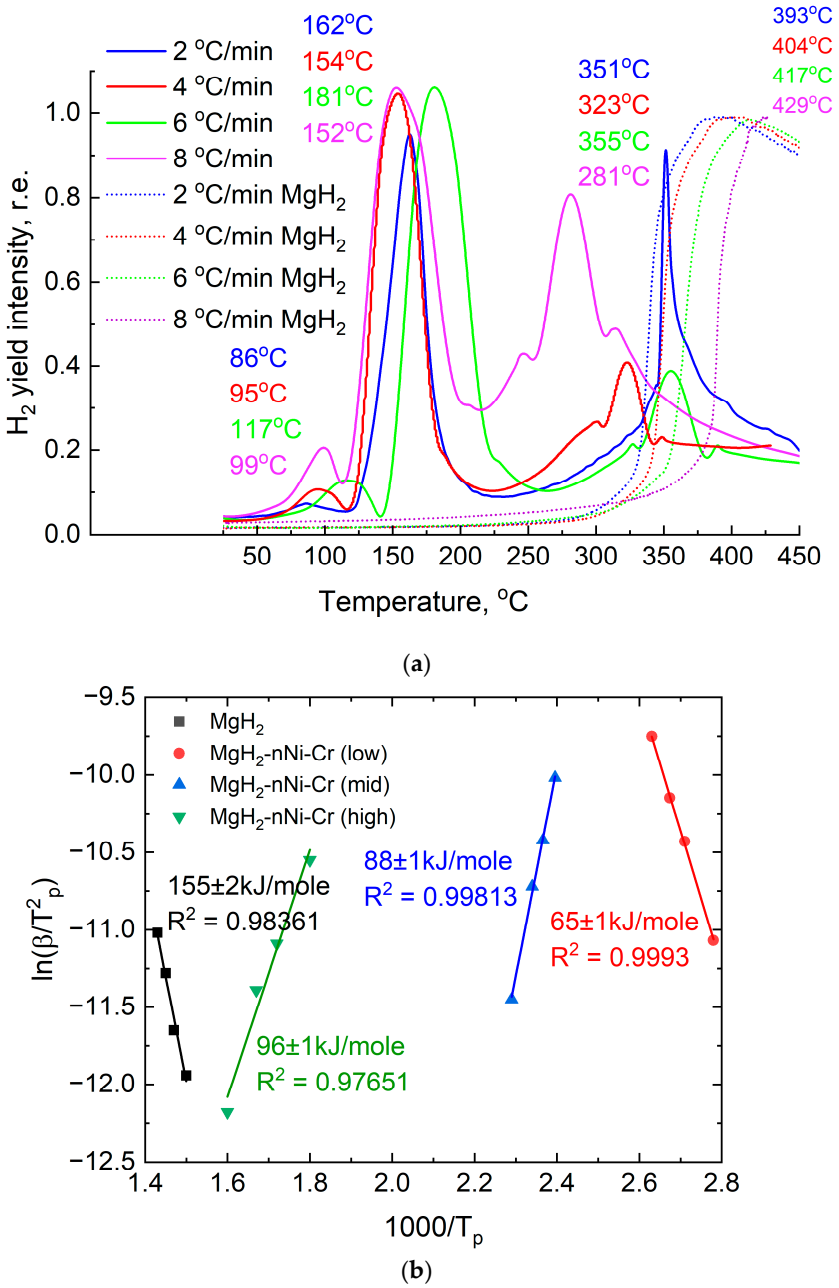


Figure 7. Temperature-programmed desorption of hydrogen for MgH_2 and the MgH_2–EEWNi-Cr composite (**a**); the relationship between $ln\frac{\beta}{T_p^2}$ and $\frac{1000}{T_p}$ for pure MgH_2 and composite MgH_2–EEWNi-Cr (**b**).

The Kissinger method (Table 4) is an overwhelmingly popular way of estimating the activation energy of thermally stimulated processes. The essence of the method is to remove these desorption curves at different heating rates (in this case—2, 4, 6, 8 °C/min), resulting in peak shifts. For the most accurate calculation of desorption activation energy using this method, a minimum of 3–5 heating rates is required, which we used in this study. It is also necessary to have a sufficiently accurate value of the heating rate of the material in relation to the values of hydrogen yield temperatures and their intensity, which is achieved by the availability of high-precision measuring and heating equipment.

Table 4. Calculation of desorption activation energy by Kissinger method.

№	Sample	β, °C/min	T_P, K	$ln\frac{\beta}{T_P^2}$	$\frac{1000}{T_p}$,	A, Angular Coefficient	Activation Energy of Desorption, kJ/mol
1	MgH_2	2	666	−11.94	1.5	−15.75	155 ± 2
		4	677	−11.65	1.47		
		6	690	−11.28	1.45		
		8	700	−11.02	1.43		
2 (low)		2	359	−11.07	2.78	−10.66	65 ± 1
		4	368	−10.43	2.71		
		6	390	−10.14	2.56		
		8	372	−9.75	2.68		
3 (mid)	MgH_2-EEWNi-Cr	2	435	−11.45	2.29	16.19	88 ± 1
		4	427	−10.72	2.34		
		6	454	−10.44	2.20		
		8	425	−10.02	2.35		
4 (high)		2	624	−12.18	1.60	7.98	96 ± 1
		4	596	−11.39	1.67		
		6	628	−11.09	1.59		
		8	554	−10.55	1.80		

We relate the three temperature regions in which hydrogen is released from the material to a complex of effects consisting of changes in the specific surface area of the material and changes in its lattice and electronic structures in the presence of a Ni-Cr catalyst:

1. We attribute the low-temperature hydrogen desorption peak at 86–117 °C mainly to surface dissociation of the hydride and the catalytic effect.
2. The hydrogen yield at 152–162 °C is also associated with the catalytic effect of the added material, but the width of the peak and its intensity suggest a bulk decomposition of the hydride phase in the material.
3. Hydrogen desorption at 281–351 °C is associated with the full dissociation of the magnesium hydride phase in the composite material, which was subsequently confirmed by the results of In situ XRD in Figure 8 below.

Similar thermodynamic effects can be observed in other studies [54,55]. The temperature values at peaks at different heating rates are taken, a calculation is performed to construct Arrhenius coordinates ($1000/T_p$ from $ln(\beta/T^2{}_p)$), and the angular coefficient (A) is determined, which gives the activation energy (E_d):

$$ln\frac{\beta}{T_P^2} = A - \frac{E_d}{RT_p}, \quad (2)$$

where A—angular coefficient, R—universal gas constant, β—heating rate, T_p—temperature of the peak hydrogen yield.

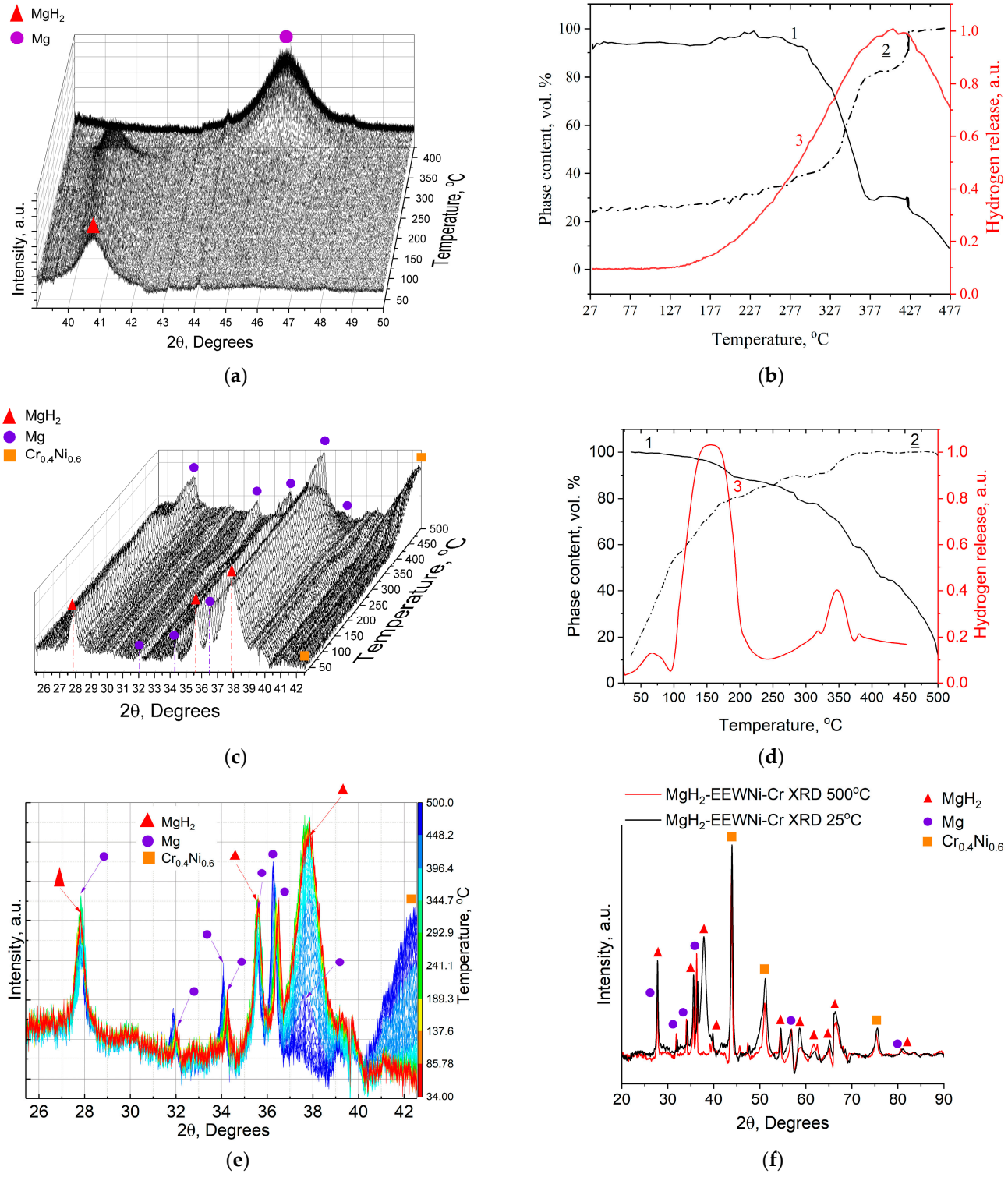


Figure 8. In situ XRD pattern, obtained In situ during heating for (**a**) MgH_2 and (**c**) MgH_2-EEWNi-Cr; graph of phase transformations during heating: 1—decrease in the MgH_2 phase, 2—increase in the Mg phase, 3—thermal-stimulated desorption for (**b**) MgH_2 and (**d**) MgH_2-EEWNi-Cr, (**e**) In situ XRD front view, comparison of non-dehydrated and dehydrated composite (**f**).

The calculated desorption activation energies for the three temperature regions were 65, 88, and 96 ± 1 kJ/mol. The strong catalytic effect of nickel–chromium powder reduced the energy required for the decomposition of the hydride phase of the material. According to the data obtained from the RHEN602 hydrogen analyzer, the hydrogen content values

in magnesium hydride and the composite material were 7.2 ± 0.2 and 5.2 ± 0.1 wt.%, respectively.

Figure 8 is an In situ X-ray phase analysis (In situ XRD) during step heating at a rate of 5 K/min from 25 to 500 °C with a dwell time at each step of 60 s (measurement time).

Figure 8a,d clearly show the change in the *β*-MgH hydride phase in MgH_2. The decrease in the hydride phase is provoked by heating of the material with further dissociation of the hydride phase, as shown in Figure 8b,d. In addition to the phase composition change, Figure 8b,d also show the thermal-stimulated desorption spectra at a heating rate of 6 K/min from 25 to 500 °C for MgH_2 and the MgH_2-EEWNi-Cr composite (20 wt.%). The main hydrogen release occurs at a temperature maximum of 150 °C for the composite (Figure 8d, third line), while for magnesium hydride this value is 417 °C (Figure 8b, third line). From Figure 8b,d, the shift of the crossing point of the phase change lines (1 and 2) during the hydrogenation/dehydrogenation process is well observed. For the initial magnesium hydride, this value is around 327 °C, while for the composite it is around 250 °C, which is presumably due to the enhancement of the thermodynamic characteristics of the material with the addition of EEWNi-Cr. It is observed that the hydride phase in the initial material starts active decomposition at a temperature around 300 °C, while for the composite a gradual decrease in the hydride phase can be observed, demonstrating a faster kinetics of hydrogen desorption from the material. Figure 8e,f clearly show the change in the magnesium hydride phase during heating from 25 to 500 °C. This change can be observed particularly well at 38° on the XRD pattern (Figure 8e).

In a recent study [56], several Mg_2TM-Mg_2TMHn (TM = Cr and Mn) materials were synthesized and the characteristics of hydrogen interaction with the obtained materials were investigated. For the $Mg_3(CrMnFeCoNi)_{0.2}H_x$ composite, the hydrogen capacity is 5.3 mass% with two desorption peaks: 247 and 277 °C. In [46], a magnesium hydride-based composite with 5 wt.% CrO_3 added demonstrates a reversible capacity of about 5 wt.% H_2 in the temperature range 250–270 °C at 5.9 atm. The results of the study [57] demonstrate a MgH_2 + 10 wt.% Cr composite capable of desorbing hydrogen at 200 °C and undergoing re-sorption at 28 °C. The material has a reversible capacity of 6.28 wt.% after 20 cycles at 285 °C. The initial dehydrogenation temperature in [58] for MgH_2-9 wt.% CrCoNi was significantly reduced from 325 °C to 195 °C, which is 130 °C lower than that of MgH_2 without additives. The composite released 4.84 mass% H_2 at 300 °C for 5 min and absorbed 3.19 mass% hydrogen at 100 °C for 30 min (3.2 MPa). The calculated activation energies of dehydrogenation/rehydration were reduced by 45 and 55 kJ/mol. The onset temperature of dehydrogenation became 195 °C, and the material was capable of releasing 6.02% by mass of hydrogen at 300 °C for 15 min. The results of ABINIT calculations performed in the study [59] demonstrated the properties of $Mg_{1-x-y}CrxH_2$ depending on the amount of transition metal added. It was found that the alloyed material and hydrogen atoms form weak hybridization in the structure, in contrast to pure magnesium hydride, which mainly consists of strong hybridization between hydrogen and magnesium atoms.

3.3. Influence of the Ni and Cr Additives on H-Mg Bonding

Hydrogen binding energies E_b on the (110) surface of β-MgH_2 were calculated both in the absence and in the presence of Ni and Cr adsorbates for several geometrically nonequivalent surface H sites, using Equation (1). In addition, the H–Mg bond lengths $d_{H–Mg}$ corresponding to these sites were computed. The results are presented in Tables 5 and 6, respectively.

Table 5. Hydrogen binding energies for the $Mg_{48}H_{96}$, $Mg_{48}H_{96}Ni$, $Mg_{48}H_{96}Cr$, and $Mg_{48}H_{96}NiCr$ systems.

System	Position of the H Atom Relative to the Adsorbate, as Defined in Figure 2		Hydrogen Binding Energy, eV
	Distance r from the Mass Center of the Adsorbate	Label	
$Mg_{48}H_{96}$	-	H3	1.307
		H7	1.514
$Mg_{48}H_{96}Ni$	$r < r_1$	H1	0.829
		H4	1.227
	$r_1 < r < r_2$	H5	0.798
		H7	0.969
	$r_2 < r < r_3$	H9	1.159
		H10	1.106
		H12	1.159
	$r_3 < r < r_4$	H13	1.048
		H11	1.139
$Mg_{48}H_{96}Cr$	$r < r_1$	H1	1.071
		H4	1.369
	$r_1 < r < r_2$	H5	0.461
		H3	0.227
	$r_2 < r < r_3$	H7	0.089
		H9	0.918
	$r \approx r_4$	H11	1.363
$Mg_{48}H_{96}NiCr$	$r < r_1$	H1	1.009
		H2	0.384
		H3	0.922
		H4	0.482
	$r_1 < r < r_2$	H5	0.729
		H6	0.626
		H7	0.208
	$r_2 < r < r_3$	H8	0.695
		H9	1.016
		H10	−0.624
	$r \approx r_5$	H11	0.770

Table 6. The range of H–Mg bond lengths on the (110) surface of the $Mg_{48}H_{96}$, $Mg_{48}H_{96}Ni$, $Mg_{48}H_{96}Cr$, and $Mg_{48}H_{96}NiCr$ systems.

Atom H	d_{H-Mg}, Å			
	$Mg_{48}H_{96}$	$Mg_{48}H_{96}Ni$	$Mg_{48}H_{96}Cr$	$Mg_{48}H_{96}NiCr$
H1	1.937–1.988	1.964–2.335	2.117–2.927	2.037–2.392
H2	1.937–1.988	1.886–1.970	2.117–2.927	1.899–2.983
H3	1.865–1.865	2.014–2.278	1.867–1.914	2.005–2.137
H4	1.865–1.865	2.014–2.278	1.987–1.987	1.989–2.055
H5	1.937–1.988	1.914–1.994	1.885–1.930	1.893–1.911
H6	1.937–1.988	1.926–1.994	1.885–1.930	1.888–1.998
H7	1.937–1.988	1.837–1.957	1.958–2.025	1.927–1.984
H8	1.937–1.988	1.960–2.078	1.926–2.025	1.895–1.934
H9	1.865–1.865	2.064–2.089	1.947–2.089	1.977–2.008
H10	1.865–1.865	2.064–2.089	1.869–1.877	1.864–1.874
H11	1.937–1.988	1.879–2.000	1.945–2.036	1.879–1.992
H12	1.865–1.865	1.885–1.885	1.867–1.914	1.858–1.898
H13	1.937–1.988	1.895–1.957	1.954–1.991	1.933–1.943

As evidenced by the data in Table 5, the hydrogen binding energies of all Ni/Cr-modified (110) β-MgH_2 systems are lower, reaching negative values, compared to the pristine surface. A distinctive feature of the $Mg_{48}H_{96}NiCr$ system, containing a surface Ni–Cr complex, is the emergence of a single negative hydrogen binding energy value (at the H10 site) among all the $Mg_{48}H_{96}$, $Mg_{48}H_{96}Ni$, $Mg_{48}H_{96}Cr$, and $Mg_{48}H_{96}NiCr$ system configurations considered. A negative binding energy indicates that, for this specific hydrogen atom, formation of a H_2 molecule is energetically more favorable than remaining adsorbed on the (110) $Mg_{48}H_{96}NiCr$ surface. Consequently, such hydrogen atoms are expected to desorb significantly earlier with increasing temperature. Furthermore, adsorption of the Ni–Cr complex leads to a pronounced reduction in all hydrogen binding energies. Notably, in the $Mg_{48}H_{96}NiCr$ configuration, binding energies for the majority of surface hydrogen atoms fall below 1 eV, which is not observed in any of the other systems considered, thereby positioning $Mg_{48}H_{96}NiCr$ as a uniquely reactive surface with enhanced hydrogen release propensity.

A common feature across all the systems considered is that hydrogen atoms with the lowest binding energy E_b are located within an intermediate radial range from the adsorbate center of mass ($r_1 < r < r_3$). At the same time, each region in Figure 2 also contains hydrogen atoms with moderately higher binding energies (1.0–1.4 eV), comparable to those on the pristine surface. At larger distances from the adsorbates ($r > r_4$), the elevated hydrogen binding energies are consistent with a reduced perturbation of the surface electronic structure, as the influence of Ni and Cr becomes negligible. In contrast, the high binding energies observed for hydrogen atoms located in close proximity to the adsorbates ($r < r_4$) can be attributed to a spatial redistribution of valence charge density induced by the presence of Ni and Cr atoms.

The computed H–Mg bond lengths $d_{H–Mg}$ (Table 6) for hydrogen atoms at positions H1–H13 exhibit a consistent increase in the presence of Ni and Cr adsorbates. This increase is more pronounced for hydrogen atoms located near the adsorbates and becomes less significant at greater distances, indicating a distance-dependent weakening of the adsorbate-induced structural perturbation.

To provide insight into the origin of H–Mg bond weakening in the presence of adsorbed Ni and Cr atoms, the valence electron density distribution was analyzed for the pristine β-MgH_2 (110) surface, as well as for surfaces modified by single Ni and Cr atoms and by the Ni–Cr complex (Figure 9). The Bader charge transfer was also calculated; it is marked by numbers in Figure 9. It is expressed in units of elementary charge and characterizes the amount of charge transferred to the atom during bond formation.

Bader charge transfer (Δq) analysis reveals that on the pristine (110) surface of β-MgH_2 the bonding between Mg and H atoms is predominantly ionic in character. The calculated transfer values Δq are approximately +1.6e for Mg and –0.8e for H atoms, which clearly indicates strong electron transfer from hydrogen to magnesium. This finding is consistent with the valence electron density distribution, where regions of electron density greater than 0.02 $e/Å^3$ are concentrated around hydrogen atoms and do not extend toward Mg atoms. The pronounced ionicity of the H–Mg interaction contributes to its high bond strength; therefore, a shift toward a more covalent character may result in a weakening of the bond.

In the $Mg_{48}H_{96}Ni_xCr_y$ systems, high valence electron density isosurfaces of 0.05 $e/Å^3$ indicate the formation of covalent bonds between the adsorbed Ni and Cr atoms and their nearest hydrogen neighbors. The size of high-density regions around the hydrogen atoms nearest to the Ni-Cr complex (at a distance less than r_1) is slightly reduced compared to the pristine surface (Figure 9a) or to the surfaces with a single Ni or Cr atom (Figure 9b,c). This size reduction and this increase in H–Mg bond lengths reflect a suppression of charge

localization, implying that the presence of the Ni–Cr complex noticeably decreases the ionic character of H–Mg bonds near the adsorbate atoms.

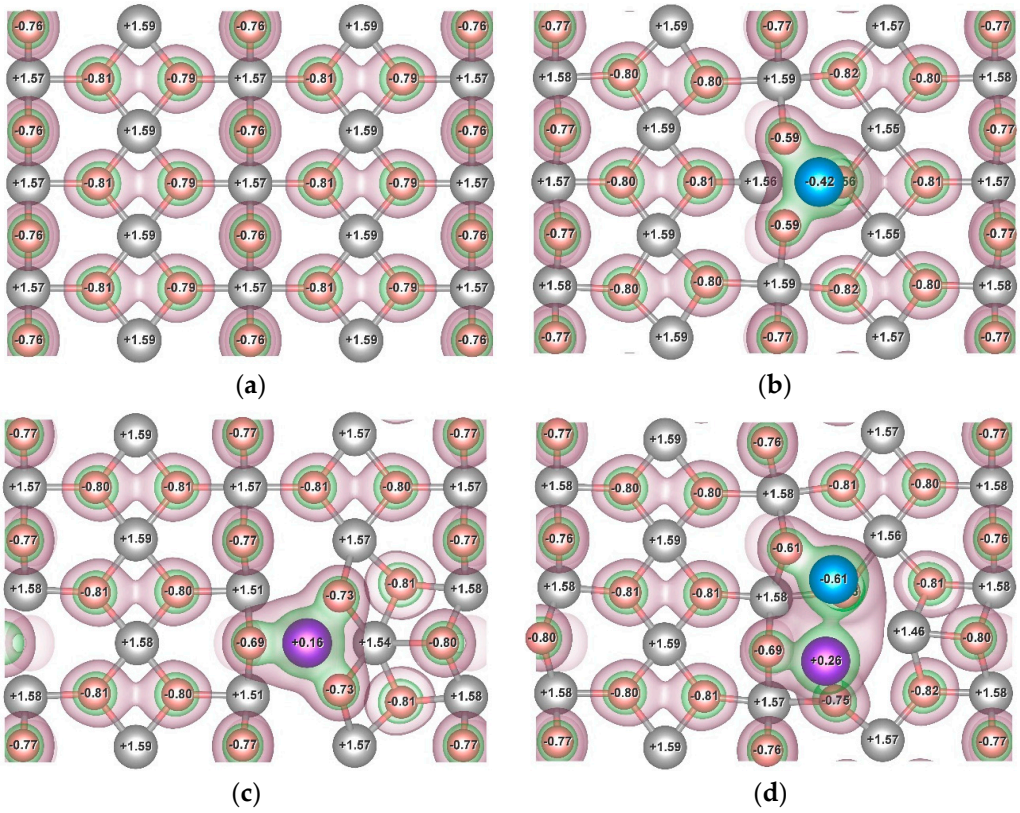


Figure 9. The valence electron density distribution and Bader charge transfer Δq on atoms on the pristine (110) surface on β-MgH_2 (**a**), and of β-MgH_2 (110) surfaces with an adsorbed Ni atom (**b**), Cr atom (**c**), and Ni–Cr complex (**d**). The atoms of Mg, H, Ni, and Cr are colored as gray, pink, blue, and purple, respectively. Isosurfaces corresponding to electron densities of 0.02 $e/Å^3$ and 0.05 $e/Å^3$ are shown in burgundy and green, respectively.

The adsorption of individual Ni or Cr atoms on the MgH_2 surface leads to the formation of predominantly covalent bonds with nearby hydrogen atoms, which in turn weakens the H–Mg interaction. As a result, the binding energy of hydrogen atoms in the vicinity of the adsorbate is reduced compared to that on the pristine MgH_2 surface. In the case of co-adsorption, Bader charge analysis shows that the charge transfer on the Ni and Cr atoms increases from –0.42*e* to –0.61*e* and from +0.16*e* to +0.26*e*, respectively. In addition, the valence electron density map (Figure 9d) reveals a common high-density isosurface (0.05 $e/Å^3$) between Cr and Ni, confirming the formation of a covalent Cr-Ni bond. This predominantly covalent interaction, together with a formation of Ni–H and Cr–H covalent bonds, leads to a redistribution of the valence electron density on the MgH_2 surface and a reduction in the ionic character of the H–Mg bonding. The decrease in hydrogen binding energy observed in the presence of the Ni–Cr complex is significantly more pronounced than in either single-element system. This synergistic effect is consistent with experimental observations, where co-milling of Ni-Cr nanosized powder and magnesium hydride leads to the emergence of a double low-temperature hydrogen desorption peak. Accordingly, surface hydrogen atoms with negative binding energies are expected to desorb first and correspond to the low-temperature desorption peak, whereas hydrogen atoms with positive binding energies desorb at higher temperatures and account for the second peak.

Hydrogen PCT (a) curves and cycles of hydrogen sorption and desorption at a temperature of 200 °C (b) for the MgH_2–EEWNi-Cr composite at different temperatures are

presented in Figure 10. Before cycling testing, the composite was dehydrogenated at 200 °C for 1 h. After conducting a series of cyclic hydrogenation/dehydrogenation tests, it was established that the material retains practically all of its initial hydrogen capacity. Further measurements are planned in order to obtain the most complete and accurate results (Figure 10).

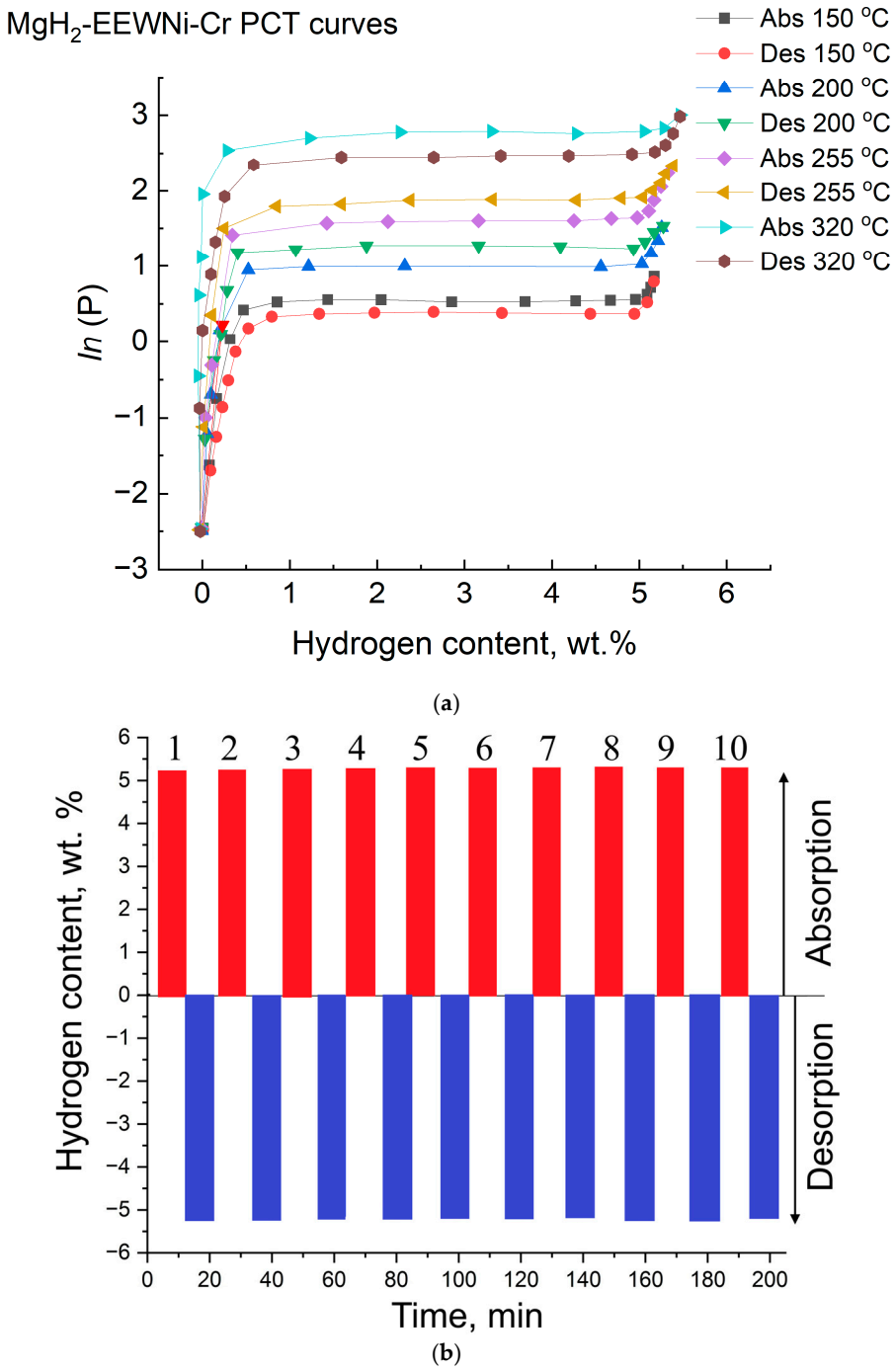


Figure 10. Pressure–Constant–Temperature (PCT) curves (**a**) and hydrogen absorption–desorption cycling curves for the MgH_2–EEWNi-Cr composite, determined at a temperature of 200 °C (**b**).

The obtained PCT curves are characterized by a slight slope, which is associated with sorption and desorption processes at different temperatures. At the same time, thermodynamic processes in the composite material proceed faster and at lower temperatures. The maximum amounts of hydrogen absorbed by the material at 150, 200, 255, and 320 °C were

5.16, 5.25, 5.38, and 5.46 mass%, respectively. These values are logically lower than for pure magnesium hydride, which was studied in our previous work [60], due to the addition of EEWNi-Cr powder. This has also established that the composite is characterized by lower-temperature sorption and, after 10 cyclic tests, it practically does not lose its initial hydrogen capacity. The amount of hydrogen in the magnesium hydride was 7.2 wt.%, while in the composite this value was 5.2 wt.%.

In the future, we plan to conduct a series of measurements consisting of 50, 100, and 500 cycles. This will allow us to clearly determine the actual effectiveness of the material relative to others.

4. Discussion

The material based on magnesium hydride and EEWNi-Cr powder obtained in this work has potential for further study and future use in mobile hydrogen storage systems in the field of hydrogen energy. Further research will focus on developing a metal hydride cell filled with the material studied in this article. This cell will be used as a source for storing and transporting hydrogen in a bound state. This will enable hydrogen to be stored safely and efficiently for its usage as a fuel. Figure 11 shows graphs of the dependence of ln (P) on 1000/T, representing the efficiency of various materials depending on their hydrogen yield temperature.

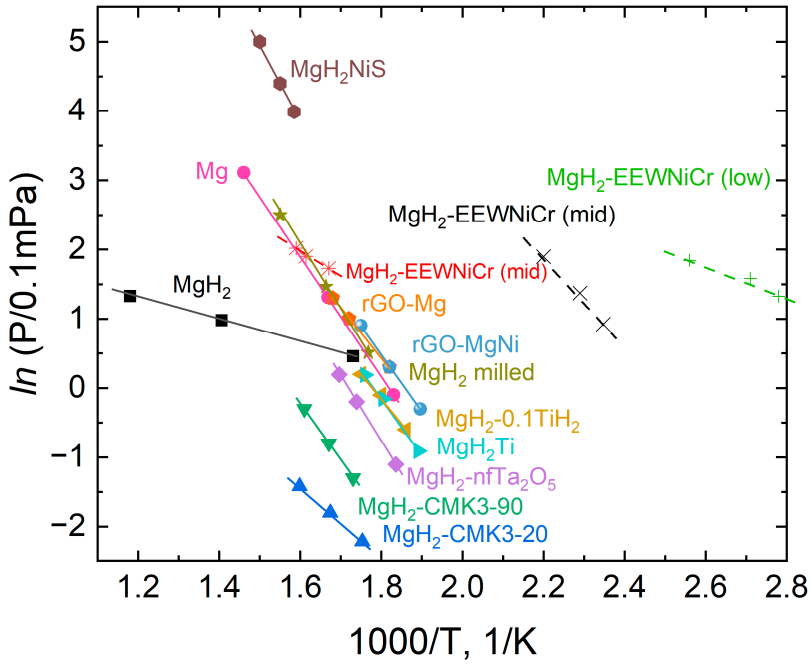


Figure 11. Comparison of the effectiveness of composites for hydrogen storage.

As can be seen from the data presented above, the composite material studied in this work is located to the right on the graph. This indicates effective dissociation of the material under the influence of temperature. The MgH_2-EEWNi-Cr material has unique thermodynamic characteristics and allows for easy scaling of the material production technology. Despite the decrease in the initial hydrogen capacity of the material from 7.2 to 5.2 wt.%, it remains high enough for use in mobile hydrogen storage systems.

The most relevant challenges at present are as follows:

- Reducing the cost of producing hydrogen, which will be environmentally friendly.
- Research and development in the field of storage and transportation.

- Cooperation between countries to improve the current state of hydrogen energy in the world.
- Investment in the development and implementation of new production technologies [61].

In combination with all the advantages of this material over others listed in this study, its use is limited only by the lack of cyclic testing. At present, there is a plan to conduct all the missing studies to provide the most comprehensive characterization of the material.

5. Conclusions

The composite MgH_2-EEWNi-Cr (20 wt.%) with hydrogen mass content of 5.2 ± 0.1 wt.% described in this work was synthesized in a planetary ball mill and described using XRD, SEM, EDX, BET, TPD, and DFT analyses. Despite the decrease in the hydrogen capacity of the studied composite material compared to pure magnesium hydride (with hydrogen mass content of 7.2 ± 0.3 wt.%), its hydrogen desorption characteristics have been significantly improved due to the catalytic effect exerted by the added material, as well as due to ball milling.

The composite is characterized by three desorption peaks in different temperature ranges. The presence of three temperature regions is explained by the catalytic effect of the added material. The desorption temperature at a heating rate of 2 °C/min was 86 °C (compared to MgH_2—393 °C), which is due to the direct participation of nickel–chromium powder, as well as additional milling with balls and nanoscale particles of the powder itself, which in turn affects the change in the specific surface area. Additional diffusion paths in the crystal lattice of the material make it easier to bind magnesium atoms with hydrogen. The dissociation of the hydride phase in the composite occurs above 250 °C. According to the Kissinger method, the activation energy of desorption is determined to be (65–96) ± 1 kJ/mol, while for hydride it is 155 ± 2 kJ/mol.

Ab initio calculations show that the synergistic effect of Ni and Cr additives on the MgH_2 surface leads to a significant decrease in the hydrogen binding energy compared to pure magnesium hydride. The first peak has a double maximum of low-temperature hydrogen desorption from 70 °C to 230 °C. The presence of a double maximum is due to an uneven decrease in the strength of hydrogen–surface bonds near the additives. In addition to positive hydrogen binding energies, weak hydrogen bonds with the surface, characterized by negative binding energy, are also observed on the MgH_2 surface with Ni and Cr additives. Surface hydrogen atoms with negative binding energies are expected to desorb first and correspond to the lowest-temperature desorption peak (~90 °C), whereas hydrogen atoms with positive binding energies desorb at higher temperatures and account for the second peak (~150 °C). The decrease in the strength of the hydrogen–surface bond is caused by the formation of Ni–H and Cr–H covalent bonds, which, due to the redistribution of electron charge on the hydrogen atoms and additives, weakens the ionic bond of hydrogen with nearby magnesium atoms.

Author Contributions: Conceptualization, V.N.K.; data curation, A.K. and D.V.T.; formal analysis, A.K., D.V.T. and D.B.V.; funding acquisition, D.S.N. and E.B.K.; investigation, A.A.S.; project administration, V.N.K.; resources, E.B.K.; software, D.V.T., D.B.V. and L.A.S.; supervision, V.N.K.; validation, A.K., A.A.S., D.S.N. and E.B.K.; writing—original draft, A.K. and D.V.T.; writing—review and editing, V.N.K. and L.A.S. All authors have read and agreed to the published version of the manuscript.

Funding: This research was funded by the Governmental Program, Grant № FSWW-2024-0001.

Data Availability Statement: The raw/processed data required to reproduce these findings cannot be shared at this time as the data also form part of an ongoing study.

Acknowledgments: The scientific infrastructure for the project was organized with the support of Tomsk Polytechnic University's Priority 2030 development program.

Conflicts of Interest: The authors declare no conflicts of interest.

Abbreviations

The following abbreviations are used in this manuscript:

ABINIT	Software package, lat. Ab initio ("from the beginning")—first-principles calculations
DFT	Density functional theory
E_b	Binding energy
E_d	Desorption activation energy
EEW	Electrical explosion of wires
MPF-4	Magnesium Powder Fraction-4
GRAM50	Gas Reaction Automated Machine 50 bar
SEM	Scanning electron microscopy
EDX	Energy-dispersive X-ray spectroscopy
XRD	X-ray diffraction
BET	Brunauer–Emmet–Teller method
BJH	Barrett–Joyner–Halenda method
TPD	Temperature-programmed desorption
RGA	Residual Gas Analyzer
JCPDS	Joint Committee on Powder Diffraction Standards
HCP	Hexagonal close-packed lattice
BCC	Base-centered cubic lattice
FCC	Face-centered cubic lattice

References

1. Abdi Lanbaran, D.; Wang, C.; Wen, C.; Wu, Z.; Li, B. Modeling the Impact of Temperature-Dependent Thermal Conductivity on Hydrogen Desorption from Magnesium Hydride. *Int. J. Hydrogen Energy* **2025**, *138*, 491–508. [CrossRef]
2. Kudiiarov, V.N.; Kenzhiyev, A.; Kurdyumov, N.; Elman, R.R.; Svyatkin, L.A.; Terenteva, D.V. Superior Catalytic Activity of Nano Sized Ni Produced by Electrical Explosion of Wires towards the Hydrogen Storage of Magnesium Hydride. *Int. J. Hydrogen Energy* **2025**, *109*, 436–452. [CrossRef]
3. Wang, Y.; Mao, W.; Su, Y.; Liu, B.; Ji, W. Investigation on Explosion Overpressure and Flame Propagation Characteristics of Magnesium Hydride Dust of Different Particle Sizes. *Int. J. Hydrogen Energy* **2025**, *101*, 438–449. [CrossRef]
4. Kudiiarov, V.N.; Kenzhiyev, A.; Elman, R.R.; Kurdyumov, N.; Ushakov, I.A.; Tereshchenko, A.V.; Laptev, R.S.; Kruglyakov, M.A.; Khomidzoda, P.I. The Defect Structure Evolution in MgH_2-EEWNi Composites in Hydrogen Sorption–Desorption Processes. *Metals* **2025**, *15*, 72. [CrossRef]
5. Drawer, C.; Lange, J.; Kaltschmitt, M. Metal Hydrides for Hydrogen Storage—Identification and Evaluation of Stationary and Transportation Applications. *J. Energy Storage* **2024**, *77*, 109988. [CrossRef]
6. Kudiiarov, V.; Elman, R.; Pushilina, N.; Kurdyumov, N. State of the Art in Development of Heat Exchanger Geometry Optimization and Different Storage Bed Designs of a Metal Hydride Reactor. *Materials* **2023**, *16*, 4891. [CrossRef]
7. Khandelwal, P.; Rathi, B.; Agarwal, S.; Juyal, S.; Gill, F.S.; Kumar, M.; Saini, P.; Dixit, A.; Ichikawa, T.; Jain, A. Core-Shell Structured Ni@C Based Additive for Magnesium Hydride System towards Efficient Hydrogen Sorption Kinetics. *Int. J. Hydrogen Energy* **2025**, *107*, 74–82. [CrossRef]
8. Elman, R.; Kudiiarov, V.; Sayadyan, A.; Pushilina, N.; Leng, H. Performance Improvement of Magnesium-Based Hydrogen Storage Tanks by Using Carbon Nanotubes Addition and Finned Heat Exchanger: Numerical Simulation and Experimental Verification. *Int. J. Hydrogen Energy* **2024**, *92*, 1375–1388. [CrossRef]
9. Rathi, B.; Agarwal, S.; Shrivastava, K.; Kumar, M.; Jain, A. Recent Advances in Designing Metal Oxide-Based Catalysts to Enhance the Sorption Kinetics of Magnesium Hydride. *Int. J. Hydrogen Energy* **2024**, *53*, 131–162. [CrossRef]
10. Li, X.; Yuan, Z.; Liu, C.; Sui, Y.; Zhai, T.; Hou, Z.; Han, Z.; Zhang, Y. Research Progress in Improved Hydrogen Storage Properties of Mg-Based Alloys with Metal-Based Materials and Light Metals. *Int. J. Hydrogen Energy* **2024**, *50*, 1401–1417. [CrossRef]
11. Yan, S.; Wei, L.; Gong, Y.; Yang, K. Enhanced Hydrogen Storage Properties of Magnesium Hydride by Multifunctional Carbon-Based Materials: A Review. *Int. J. Hydrogen Energy* **2024**, *55*, 521–541. [CrossRef]

12. Kudiiarov, V.N.; Kurdyumov, N.; Elman, R.R.; Laptev, R.S.; Kruglyakov, M.A.; Ushakov, I.A.; Tereshchenko, A.V.; Lider, A.M. The Defect Structure Evolution in Magnesium Hydride/Metal-Organic Framework Structures MIL-101 (Cr) Composite at High Temperature Hydrogen Sorption-Desorption Processes. *J. Alloys Compd.* **2023**, *966*, 171534. [CrossRef]
13. Günaydın, Ö.F.; Topçu, S.; Aksoy, A. Hydrogen Fuel Cell Vehicles: Overview and Current Status of Hydrogen Mobility. *Int. J. Hydrogen Energy* **2025**, *142*, 918–936. [CrossRef]
14. Xu, H.; Zhang, Y.; Zhang, X. Towards Efficient and Safe Hydrogen Storage for Green Shipping: Progress on Critical Technical Issues of Material Development and System Construction. *Int. J. Hydrogen Energy* **2025**, *167*, 150913. [CrossRef]
15. Osman, A.I.; Ayati, A.; Farrokhi, M.; Khadempir, S.; Rajabzadeh, A.R.; Farghali, M.; Krivoshapkin, P.; Tanhaei, B.; Rooney, D.W.; Yap, P.-S. Innovations in Hydrogen Storage Materials: Synthesis, Applications, and Prospects. *J. Energy Storage* **2024**, *95*, 112376. [CrossRef]
16. Kudiiarov, V.N.; Kurdyumov, N.; Elman, R.R.; Svyatkin, L.A.; Terenteva, D.V.; Semyonov, O. Microstructure and Hydrogen Storage Properties of MgH_2/MIL-101(Cr) Composite. *J. Alloys Compd.* **2024**, *976*, 173093. [CrossRef]
17. Fang, L.; Liu, C.; Feng, Y.; Gao, Z.; Chen, S.; Huang, M.; Ge, H.; Huang, L.; Gao, Z.; Yang, W. Size-Dependent Nanoconfinement Effects in Magnesium Hydride. *Int. J. Hydrogen Energy* **2024**, *96*, 783–793. [CrossRef]
18. Żukowski, W.; Berkowicz-Płatek, G.; Wencel, K.; Migas, P.; Wrona, J.; Reyna-Bowen, L. Hydrogen Production from Liquid Organic Hydrogen Carriers in a Fluidized-Bed Made out of Co_3O_4-Cenosphere Catalyst. *Int. J. Hydrogen Energy* **2025**, *136*, 358–370. [CrossRef]
19. Yang, S.; Xu, C.; Fan, Q.; Wei, Y.; Qu, D.; Li, X.; Xie, Z.; Tang, H.; Li, J.; Liu, D. Electrochemical Hydrogen Storage in Zeolite Template Carbon and Its Application in a Proton/Potassium Hybrid Ion Hydrogel Battery Coupling with Nickel-Zinc Co-Doped Prussian Blue Analogues. *Int. J. Hydrogen Energy* **2025**, *122*, 139–149. [CrossRef]
20. Mondal, B.; Kundu, A.; Chakraborty, B. High-Capacity Hydrogen Storage in Zirconium Decorated Zeolite Templated Carbon: Predictions from DFT Simulations. *Int. J. Hydrogen Energy* **2022**, *47*, 38671–38681. [CrossRef]
21. Kashani, F.Z.; Mohsennia, M. Enhancing Electrochemical Hydrogen Storage in Nickel-Based Metal-Organic Frameworks (MOFs) through Zinc and Cobalt Doping as Bimetallic MOFs. *Int. J. Hydrogen Energy* **2025**, *101*, 348–357. [CrossRef]
22. Hu, J.-Q.; Jiang, W.; Si, N.; Wang, Z.; Zhang, H. MOF-Derived Carbon Supported Transition Metal (Fe, Ni) and Synergetic Catalysis for Hydrogen Storage Kinetics of MgH_2. *Int. J. Hydrogen Energy* **2024**, *86*, 445–455. [CrossRef]
23. Zhang, X.; Zheng, Q.; He, H. Synergistic Effect of Hydrogen Spillover and Nano-Confined AlH3 on Room Temperature Hydrogen Storage in MOFs: By GCMC, DFT and Experiments. *Int. J. Hydrogen Energy* **2024**, *72*, 1224–1235. [CrossRef]
24. Gao, H.; Shi, R.; Shao, Y.; Liu, Y.; Zhu, Y.; Zhang, J.; Li, L. Catalysis Derived from Flower-like Ni MOF towards the Hydrogen Storage Performance of Magnesium Hydride. *Int. J. Hydrogen Energy* **2022**, *47*, 9346–9356. [CrossRef]
25. Kushwaha, A.; Kumar, A. MOFs and MOF Derivatives for Electrocatalytic Hydrogen Evolution Reaction: Designing Strategies, Syntheses and Future Prospects. *Int. J. Hydrogen Energy* **2025**, *150*, 150148. [CrossRef]
26. Zhang, L.; Yong, H.; Wang, S.; Yan, Z.; Xu, Z.; Li, Y.; Liu, B.; Hu, J.; Zhang, Y. Investigating of Hydrolysis Kinetics and Catalytic Mechanism of Mg–Ce–Ni Hydrogen Storage Alloy Catalyzed by Ni/Co/Zn-Based MOF. *Int. J. Hydrogen Energy* **2024**, *71*, 1416–1427. [CrossRef]
27. Zhao, S.; Wu, T.; Wang, K.; Wang, Q.; Mei, X.; Huang, J.; Liu, H.; Huang, C.; Guo, J. Synergistic Dual-Modification Regulation of Dehydrogenation Kinetics of MgH_2 by MOF-Derived Core-Shell Ni&C. *Int. J. Hydrogen Energy* **2025**, *127*, 241–251. [CrossRef]
28. Yamçıçıer, Ç.; Kürkçü, C. Investigation of Structural, Electronic, Elastic, Vibrational, Thermodynamic, and Optical Properties of Mg_2NiH_4 and Mg_2RuH_4 Compounds Used in Hydrogen Storage. *J. Energy Storage* **2024**, *84*, 110883. [CrossRef]
29. Kapsi, M.; Veziri, C.M.; Pilatos, G.; Karanikolos, G.N.; Romanos, G.E. Zeolite-Templated Sub-Nanometer Carbon Nanotube Arrays and Membranes for Hydrogen Storage and Separation. *Int. J. Hydrogen Energy* **2022**, *47*, 36850–36872. [CrossRef]
30. Wen, Y.; Chai, X.; Gu, Y.; Wu, W.; Ma, W.; Zhang, J.; Zhang, T. Advances in Hydrogen Storage Materials for Physical H_2 Adsorption. *Int. J. Hydrogen Energy* **2025**, *97*, 1261–1274. [CrossRef]
31. Worth, J.D.; Ting, V.P.; Faul, C.F.J. Exploring Conjugated Microporous Polymers for Hydrogen Storage: A Review of Current Advances. *Int. J. Hydrogen Energy* **2025**, *152*, 149718. [CrossRef]
32. Hossain Bhuiyan, M.M.; Siddique, Z. Hydrogen as an Alternative Fuel: A Comprehensive Review of Challenges and Opportunities in Production, Storage, and Transportation. *Int. J. Hydrogen Energy* **2025**, *102*, 1026–1044. [CrossRef]
33. Han, S.J.; Ramadhani, S.; Ha, T.; Kim, E.-Y.; Baek, J.; Jeong, D.; Park, G.; Kim, J.; Lee, Y.-S.; Shim, J.-H.; et al. Dual Functionality of $LaNi_5$ Metal Hydride as a Catalyst for Toluene Hydrogenation. *Int. J. Hydrogen Energy* **2025**, *167*, 150891. [CrossRef]
34. Liu, Y.; Chabane, D.; Elkedim, O. Optimization of LaNi5 Hydrogen Storage Properties by the Combination of Mechanical Alloying and Element Substitution. *Int. J. Hydrogen Energy* **2024**, *53*, 394–402. [CrossRef]
35. Thiangviriya, S.; Thongtan, P.; Thaweelap, N.; Plerdsranoy, P.; Utke, R. Heat Charging and Discharging of Coupled MgH_2–$LaNi_5$ Based Thermal Storage: Cycling Stability and Hydrogen Exchange Reactions. *Int. J. Hydrogen Energy* **2024**, *49*, 59–66. [CrossRef]
36. Arslan, B.; Ilbas, M.; Celik, S. Experimental Analysis of Hydrogen Storage Performance of a $LaNi_5$–H_2 Reactor with Phase Change Materials. *Int. J. Hydrogen Energy* **2023**, *48*, 6010–6022. [CrossRef]

37. Chibani, A.; Boucetta, C.; Haddad, M.A.N.; Boukhari, A.; Fourar, I.; Merouani, S.; Badji, R.; Adjel, S.; Belkhiria, S.; Boukraa, M.; et al. A Novel Metal Hydride Reactor Design: The Effect of Using Copper, AlN and AlSi10Mg Composite Fins on the Dehydrogenation Process of $LaNi_5$-Metal Alloy. *Int. J. Hydrogen Energy* **2025**, *141*, 118–132. [CrossRef]
38. Chandra Mouli, B.; Sharma, V.K.; Paswan, M.; Thomas, B. Performance Investigations on Thermochemical Energy Storage System Using Cerium, Aluminium, Manganese, and Tin-Substituted $LaNi_5$ Hydrides. *Int. J. Hydrogen Energy* **2024**, *96*, 1203–1214. [CrossRef]
39. Eikeng, E.; Makhsoos, A.; Pollet, B.G. Critical and Strategic Raw Materials for Electrolysers, Fuel Cells, Metal Hydrides and Hydrogen Separation Technologies. *Int. J. Hydrogen Energy* **2024**, *71*, 433–464. [CrossRef]
40. Parviz, R.; Heydarinia, A.; Nili-Ahmadabadi, M. Enhanced Hydrogen Storage via In-Situ Formation of Oxide, Metallic and Intermetallic Catalysts in a Mg-Based Porous-Layered Composite. *Int. J. Hydrogen Energy* **2025**, *111*, 220–227. [CrossRef]
41. Aguiar, V.B.; Júnior, W.O.; Gonzalez Cruz, E.D.; Leiva, D.R.; Pereira Da Silva, E. Casting of Mg-Based Alloy with Ni and Mishmetal Addition ($Mg_{88}Ni_8MM_4$) for Hydrogen Storage. *Int. J. Hydrogen Energy* **2025**, *109*, 63–66. [CrossRef]
42. Nivedhitha, K.S.; Banapurmath, N.R.; Yaliwal, V.S.; Umarfarooq, M.A.; Sajjan, A.M.; Venkatesh, R.; Hosmath, R.S.; Beena, T.; Yunus Khan, T.M.; Kalam, M.A.; et al. From Nickel–Metal Hydride Batteries to Advanced Engines: A Comprehensive Review of Hydrogen's Role in the Future Energy Landscape. *Int. J. Hydrogen Energy* **2024**, *82*, 1015–1038. [CrossRef]
43. Liu, C.; Yuan, Z.; Li, X.; Man, X.; Zhai, T.; Han, Z.; Li, T.; Zhang, Y. Hydrogen Storage Capabilities Enhancement of MgH_2 Nanocrystals. *Int. J. Hydrogen Energy* **2024**, *88*, 515–527. [CrossRef]
44. Polanski, M.; Bystrzycki, J.; Varin, R.A.; Plocinski, T.; Pisarek, M. The Effect of Chromium (III) Oxide (Cr_2O_3) Nanopowder on the Microstructure and Cyclic Hydrogen Storage Behavior of Magnesium Hydride (MgH_2). *J. Alloys Compd.* **2011**, *509*, 2386–2391. [CrossRef]
45. Polanski, M.; Bystrzycki, J. Comparative Studies of the Influence of Different Nano-Sized Metal Oxides on the Hydrogen Sorption Properties of Magnesium Hydride. *J. Alloys Compd.* **2009**, *486*, 697–701. [CrossRef]
46. Pukazhselvan, D.; Çaha, I.; De Lemos, C.; Mikhalev, S.M.; Deepak, F.L.; Fagg, D.P. Understanding the Catalysis of Chromium Trioxide Added Magnesium Hydride for Hydrogen Storage and Li Ion Battery Applications. *J. Magnes. Alloys* **2024**, *12*, 1117–1130. [CrossRef]
47. Nivedhitha, K.S.; Beena, T.; Banapurmath, N.R.; Umarfarooq, M.A.; Ramasamy, V.; Soudagar, M.E.M.; Ağbulut, Ü. Advances in Hydrogen Storage with Metal Hydrides: Mechanisms, Materials, and Challenges. *Int. J. Hydrogen Energy* **2024**, *61*, 1259–1273. [CrossRef]
48. Zhang, W.; Zhao, D.; Li, J.; Yuan, Z.; Guo, S.; Qi, Y.; Zhang, Y. Hydrogen Storage Property Improvement of La–Y–Mg–Ni Alloy by Ball Milling with TiF_3. *Int. J. Hydrogen Energy* **2023**, *48*, 17957–17969. [CrossRef]
49. Song, F.; Yao, J.; Yong, H.; Wang, S.; Xu, X.; Chen, Y.; Zhang, L.; Hu, J. Investigation of Ball-Milling Process on Microstructure, Thermodynamics and Kinetics of Ce–Mg–Ni-Based Hydrogen Storage Alloy. *Int. J. Hydrogen Energy* **2023**, *48*, 11274–11286. [CrossRef]
50. Gonze, X.; Amadon, B.; Antonius, G.; Arnardi, F.; Baguet, L.; Beuken, J.-M.; Bieder, J.; Bottin, F.; Bouchet, J.; Bousquet, E.; et al. The Abinitproject: Impact, Environment and Recent Developments. *Comput. Phys. Commun.* **2020**, *248*, 107042. [CrossRef]
51. Romero, A.H.; Allan, D.C.; Amadon, B.; Antonius, G.; Applencourt, T.; Baguet, L.; Bieder, J.; Bottin, F.; Bouchet, J.; Bousquet, E.; et al. ABINIT: Overview and Focus on Selected Capabilities. *J. Chem. Phys.* **2020**, *152*, 124102. [CrossRef] [PubMed]
52. Perdew, J.P.; Burke, K.; Ernzerhof, M. Generalized Gradient Approximation Made Simple. *Phys. Rev. Lett.* **1996**, *77*, 3865–3868. [CrossRef]
53. Bader, R.F.W. *Atoms in Molecules: A Quantum Theory*; Oxford University Press: Oxford, UK, 1990; ISBN 978-0-19-855168-3.
54. Rzeszotarska, M.; Dworecka-Wójcik, J.; Dębski, A.; Czujko, T.; Polański, M. Magnesium-Based Complex Hydride Mixtures Synthesized from Stainless Steel and Magnesium Hydride with Subambient Temperature Hydrogen Absorption Capability. *J. Alloys Compd.* **2022**, *901*, 163489. [CrossRef]
55. Ni, J.; Zhu, Y.; Zhang, J.; Ma, Z.; Liu, Y.; Wang, A.; Li, L. Air Exposure Improving Hydrogen Desorption Behavior of Mg–Ni-Based Hydrides. *Int. J. Hydrogen Energy* **2023**, *48*, 22183–22191. [CrossRef]
56. Pericoli, E.; Barzotti, A.; Mazzaro, R.; Moury, R.; Cuevas, F.; Pasquini, L. Synthesis and Hydrogen Storage Properties of Mg-Based Complex Hydrides with Multiple Transition Metal Elements. *ACS Appl. Energy Mater.* **2025**, *8*, 4993–5003. [CrossRef]
57. Wang, L.; Zhang, L.; Wu, F.; Jiang, Y.; Yao, Z.; Chen, L. Promoting Catalysis in Magnesium Hydride for Solid-State Hydrogen Storage through Manipulating the Elements of High Entropy Oxides. *J. Magnes. Alloys* **2024**, *12*, 5038–5050. [CrossRef]
58. Li, S.; Wu, F.; Zhang, Y.; Zhou, R.; Lu, Z.; Jiang, Y.; Bian, T.; Shang, D.; Zhang, L. Enhanced Hydrogen Storage Performance of Magnesium Hydride Catalyzed by Medium-Entropy Alloy CrCoNi Nanosheets. *Int. J. Hydrogen Energy* **2024**, *50*, 1015–1024. [CrossRef]
59. Bahou, S.; Labrim, H.; Ez-Zahraouy, H. Role of Vacancies and Transition Metals on the Thermodynamic Properties of MgH_2: Ab-Initio Study. *Int. J. Hydrogen Energy* **2023**, *48*, 8179–8188. [CrossRef]

60. Kudiiarov, V.; Elman, R.; Kurdyumov, N.; Laptev, R. The phase transitions behavior and defect structure evolution in magnesium hydride/single-walled carbon nanotubes composite at hydrogen sorption-desorption processes. *J. Alloys Compd.* **2023**, *953*, 170138. [CrossRef]
61. Ahmad, S.; Ullah, A.; Samreen, A.; Qasim, M.; Nawaz, K.; Ahmad, W.; Alnaser, A.; Kannan, A.M.; Egilmez, M. Hydrogen Production, Storage, Transportation and Utilization for Energy Sector: A Current Status Review. *J. Energy Storage* **2024**, *101*, 113733. [CrossRef]

Disclaimer/Publisher's Note: The statements, opinions and data contained in all publications are solely those of the individual author(s) and contributor(s) and not of MDPI and/or the editor(s). MDPI and/or the editor(s) disclaim responsibility for any injury to people or property resulting from any ideas, methods, instructions or products referred to in the content.